NanoFe$_3$O$_4$ as Solid Electron Shuttles to Accelerate Acetotrophic Methanogenesis by *Methanosarcina barkeri*

Li Fu[1,2], Ting Zhou[1], Jingyuan Wang[1], Lexing You[1], Yahai Lu[2], Linpeng Yu[1]* and Shungui Zhou[1]*

[1] Fujian Provincial Key Laboratory of Soil Environmental Health and Regulation, College of Resources and Environment, Fujian Agriculture and Forestry University, Fuzhou, China, [2] College of Urban and Environmental Sciences, Peking University, Beijing, China

Magnetite nanoparticles (nanoFe$_3$O$_4$) have been reported to facilitate direct interspecies electron transfer (DIET) between syntrophic bacteria and methanogens thereby improving syntrophic methanogenesis. However, whether or how nanoFe$_3$O$_4$ affects acetotrophic methanogenesis remain unknown. Herein, we demonstrate the unique role of nanoFe$_3$O$_4$ in accelerating methane production from direct acetotrophic methanogenesis in *Methanosarcina*-enriched cultures, which was further confirmed by pure cultures of *Methanosarcina barkeri.* Compared with other nanomaterials of higher electrical conductivity such as carbon nanotubes and graphite, nanoFe$_3$O$_4$ with mixed valence Fe(II) and Fe(III) had the most significant stimulatory effect on methane production, suggesting its redox activity rather than electrical conductivity led to enhanced methanogenesis by *M. barkeri*. Cell morphology and spectroscopy analysis revealed that nanoFe$_3$O$_4$ penetrated into the cell membrane and cytoplasm of *M. barkeri*. These results provide the unprecedented possibility that nanoFe$_3$O$_4$ in the cell membrane of methanogens serve as electron shuttles to facilitate intracellular electron transfer and thus enhance methane production. This work has important implications not only for understanding the mechanisms of mineral-methanogen interaction but also for optimizing engineered methanogenic processes.

Keywords: magnetite nanoparticle, acetotrophic methanogenesis, *Methanosarcina barkeri*, electron shuttles, wetland

INTRODUCTION

Acetate is a major intermediate product in the anaerobic digestion process and can be further metabolized by direct or syntrophic pathways to form CH$_4$, the end product of anaerobic digestion. In the syntrophic pathway, acetate is oxidized to H$_2$ and CO$_2$ by syntrophic acetate-oxidizing bacteria, and H$_2$ is consumed by hydrogenotrophic methanogens to generate CH$_4$ (Schnürer et al., 1999). The syntrophic pathway often dominates in thermophilic anaerobic digesters (Hao et al., 2010). In the direct pathway, acetotrophic methanogens like *Methanosarcina* and *Methanosaeta* convert acetate into CH$_4$ and CO$_2$ (Welte and Deppenmeier, 2014), which is the main acetate degradation pathway in mesophilic anaerobic digesters.

Magnetite is a common low-toxicity ferromagnetic black color iron oxide that is widely distributed on earth. Magnetite has a relatively low redox potential (-314 mV) and both Fe(II) and Fe(III) are present in its structure. There are 16 octahedral voids in the magnetite unit cell, with 8 Fe^{2+} and 8 Fe^{3+} filled in the octahedral void (Fleet, 1981). Magnetite has an excellent conductivity because Fe^{2+} and Fe^{3+} are basically disorderly arranged on the octahedron and electrons can rapidly transfer between the two oxidation states of iron. Magnetic nanoparticles (nanoFe$_3$O$_4$) have been widely used in the catalytic (Hudson et al., 2014), biomedical (Mohammed et al., 2017), and environmental fields (Mohammed et al., 2017; Su, 2017).

Magnetite has been demonstrated to stimulate methane production in enrichment cultures initiated with rice paddy soil (Lovley, 2017). The authors hypothesized that magnetite mediated direct interspecies electron transport between the *Geobacter* species and the *Methanosarcina* species to promote methane production (Kato et al., 2012). Subsequently defined coculture studies with *G. metallireducens* and *M. barkeri* validated the hypothesis that magnetite promotes DIET (Rotaru et al., 2014; Tang et al., 2016). Until now, many studies have suggested that the addition of either magnetite or other conductive materials such as graphite, activated carbon, etc., to promote DIET can significantly facilitate syntrophic methanogenesis from benzoate (Zhuang et al., 2015), butyrate (Li et al., 2015; Zhang and Lu, 2016; Fu et al., 2018), propionate (Viggi et al., 2014; Yamada et al., 2015; Jing et al., 2017), acetate (Yamada et al., 2015; Zhuang et al., 2018), or ethanol (Kato et al., 2012; Rotaru et al., 2014). How magnetite mediated DIET has been a major concern for researchers. Current evidence suggests that magnetite can partially substitute and supplement the function of the OmcS cytochrome on the pili of *G. sulfurreducens*, but it cannot substitute the pili itself (Lovley, 2017). It is undoubtedly an important discovery that magnetite exhibits the function of cytochromes that are involved in DIET. This indicates that magnetite can act as a solid-state electron shuttle to mediate DIET in syntrophic methanogenesis.

The accelerated syntrophic acetate oxidation with magnetite has been confirmed under conditions of a high ammonium concentration (Zhuang et al., 2018) or high temperature (Yamada et al., 2015). Although magnetite also accelerated the mesophilic methanogenesis from acetate (Yang et al., 2015), there are still some problems that remain not resolved. First, does magnetite make the syntrophic acetate oxidation as the dominant methanogenesis pathway? Second, can magnetite promote the direct acetotrophic methanogenesis? To address these problems, an enriched culture system was incubated with ^{13}C isotope-labeled acetate as the sole substrate to trace the active microorganisms and clarify the methanogenesis pathway. We found that magnetite played a unique role in promoting the acetotrophic methanogenesis by *Methanosarcina barkeri*, whereas carbon nanotubes (CNTs) or graphite nanoparticles with a higher electrical conductivity did not have the same capability. Pure culture experiments of *M. barkeri* were carried out to further explore the underlying mechanism of magnetite.

MATERIALS AND METHODS

Enrichment Cultivation

The surface soil samples were collected on 25 July 2012 from an open fen close to the Wetland National Nature Reserve of Zoige located in Qinghai-Tibetan Plateau (33°47′ N, 102°57′ E) (Fu et al., 2015). Enrichment cultivation was conducted in the same way as previously described (Fu et al., 2018). Enrichment incubation was initiated by inoculating 4% (v/v) pre-incubated soil slurry (21 days) into 60-mL vessels containing 25 mL of Hepes-buffered (30 mM, pH 7.0) fresh medium under a headspace of N$_2$/CO$_2$ (80/20). The basal medium contained MgCl$_2\cdot$6H$_2$O (0.4 g L^{-1}), CaCl$_2\cdot$H$_2$O (0.1 g L^{-1}), NH$_4$Cl (0.1 g L^{-1}), KH$_2$PO$_4$ (0.2 g L^{-1}), KCl (0.5 g L^{-1}), and resazurin (0.0005 g L^{-1}), and was supplemented with Na$_2$S$\cdot$9H$_2$O (1.0 mM), vitamin and trace element solutions as described previously (Lü and Lu, 2012). Sodium acetate was added to a final concentration of 5 mM in the initial four transfers and then increased to 10 mM thereafter. Cysteine was not added to avoid the possible effect of electron shuttle molecules. NanoFe$_3$O$_4$ were synthesized as described previously (Kang et al., 1996). The first transfer was inoculated from the pre-incubated soil slurry, the effect of nanoFe$_3$O$_4$ concentration (2.32, 4.64, and 6.96 mM of Fe in the medium) was determined. Continuous transfers were conducted in the presence of nanoFe$_3$O$_4$ (4.64 mM of Fe in the medium). The inocula for every transfer were taken from the later nanoFe$_3$O$_4$-amended cultivation. For a comparison, the same inocula were used to make parallel preparations without nanoFe$_3$O$_4$ in the medium (i.e., the control).

Isotope Labeling and Molecular Analysis

The final cultivation (after thirteen transfers) was used to extract microbial DNA following the previous protocol (Ma et al., 2012). Briefly, 10 mL of enrichment was extracted sequentially with TPMS buffer [50 mM Tris–HCl (pH 7.0), 1.7% (wt/vol) polyvinylpyrrolidone K25, 20 mM MgCl$_2$, 1% (wt/vol) sodium dodecyl sulfate] and phenol-based lysis (PBL) buffer [5 mM Tris–HCl (pH 7.0), 5 mM Na$_2$EDTA, 1% (wt/vol) sodium dodecyl sulfate, 6% (vol/vol) water-saturated phenol]. Beads-beating was performed in FastPrep-24 (MP Biomedicals, United States). The supernatants were further extracted with water-saturated phenol, phenol-chloroform-isoamyl alcohol [25:24:1 (vol/vol/vol)], and chloroform-isoamyl alcohol [24:1 (vol/vol)]. The extracts were purified by cold ethanol and sodium acetate.

DNA samples from both the control and nanoFe$_3$O$_4$ treatment were used to construct bacterial and archaeal clone libraries. The PCR amplification, cloning and sequencing followed the previous procedure (Kumar et al., 2016). Phylogenetic trees were constructed using the neighbor-joining algorithm of the MEGA7 program (Kumar et al., 2016), and bootstrap analysis was implemented with 1000 replicates. DNA-SIP was performed using the same cultivation. For this purpose, the sodium acetate-2-^{13}C (99 atom%; Sigma-Aldrich) was added as the substrate. At the end of incubation, the carbon isotopic ratios (δ^{13}C values) of CH$_4$ and CO$_2$ were analyzed by a gas chromatography-isotope ratio mass spectrometry system

(Fu et al., 2018). DNA was extracted from the ^{13}C-labeled and non-labeled cultivations and subjected to DNA-SIP procedure through the isopycnic centrifugation and density gradient fractionation of DNA as described previously (Rui et al., 2011). Centrifugation medium was prepared by mixing cesium trifluoroacetate (CsTFA) (Amersham Pharmacia Biotech) with gradient buffer (0.1 M Tris–HCl, pH 8; 0.1 M KCl; 1 mM EDTA). The mixtures were centrifuged in a Ti90 vertical rotor (Beckman) at 177000 g, 20°C for >36 h using Beckman Optima 2-80XP Ultracentrifuge (Beckman Coulter, United States). The density-resolved DNA was fractionated, and the buoyant density of each fraction was determined by refractometer.

The density-resolved DNA gradients were quantified for total bacteria and archaea using real-time quantitative PCR (Gan et al., 2012). Quantitative PCR of archaeal and bacterial 16S rRNA genes were carried out in a 7500 real-time PCR system (Applied Biosystems) using the primer pair Ar364/Ar934, and Ba519f/Ba907r, respectively. The fingerprinting of the DNA gradients was conducted using the terminal restriction fragment length polymorphism analysis (T-RFLP) following the protocol described previously (Liu et al., 2011). PCR amplification was performed using the primer pairs of Ba27f/Ba907r for bacteria and Ar109f/Ar934r for archaea. The 5′ end of the Ba27f and Ar934r primers were labeled with 6-carboxyfluorescein (FAM). PCR products were purified using an agarose gel DNA extraction kit (TaKaRa) and digested with *Msp* I (Takara) for bacteria and *Taq* I (Takara) for archaea, respectively.

Pure Culture Experiments

Methanosarcina barkeri (DSM800) were purchased from German culture collection DSMZ (Braunschweig, Germany). The basal medium was consistent with that described in the previous enrichment culture experiment. Sodium acetate was added to a final concentration of 10 mM. The effect of nanoFe₃O₄ was tested for pure culture strains.

Electrochemical Analysis

The redox activity was analyzed by cyclic voltammetry (CV) and electrochemical impedance spectroscopy (EIS) using the CHI660 as described previously (Zhou et al., 2018). Graphite plates (1.0 cm × 1.5 cm) and saturated calomel reference electrodes (SCE) were used as the working electrode, counter electrode and reference electrode, respectively. The CV scan parameters were as follows: initial potential was 0.6 V vs. SCE, maximum potential was 0.6 V vs. SCE, minimum potential was −0.8 V vs. SCE, termination potential was 0.6 V vs. SCE, and the scan rate was 0.015 V/s. The EIS scan had a high frequency value of 100000 Hz, a low frequency value of 0.1 Hz, and an amplitude of 0.005 V. In the electrochemical impedance test, the protoplast part of the biofilm was considered to be insulated under low frequency electrical perturbations, and the biofilm was considered as a multi-element circuit.
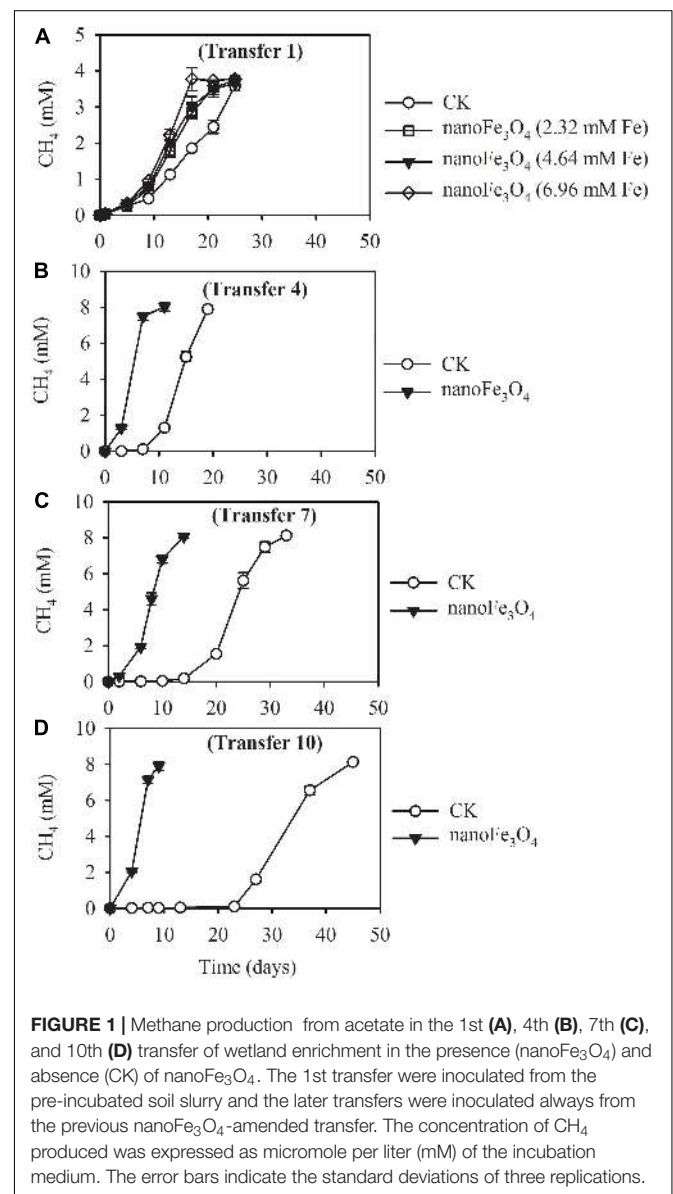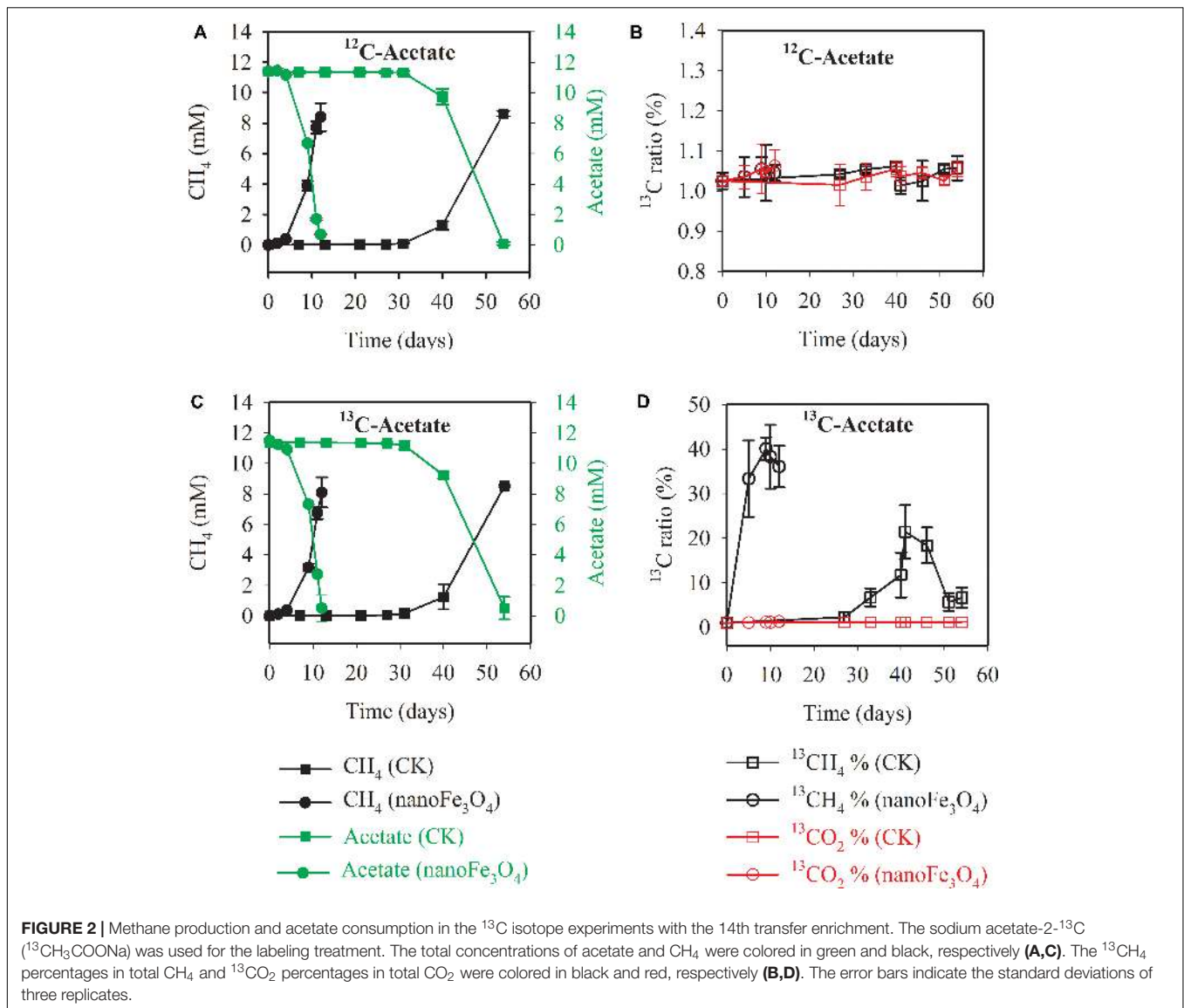
XRD and Raman Analysis

For XRD analysis, the culture was centrifuged (4000 g, 2 min). Then the supernatant was removed, and the solids were lyophilized in vacuum for 48 h. The dried sample was analyzed by a D/MAX-2400 X-ray diffractometer. The monochromatic Cu target Kα was irradiated with a current of 80 mA and a voltage of 40 kV. The acquisition range is 3–70° with an accuracy of 1.2°/min and a time of 6 s (Li et al., 2015). For Raman analysis, the centrifuged sample was air-dried under nitrogen protection until no significant aqueous layer was visible. Mineral structure and composition were analyzed using a LabRam HR800 laser confocal micro-Raman spectrometer. The excitation wavelength is 532 nm, the grating is 600 gr/mm, the objective magnification is 50 times, and the focused spot size is about 1.5 μm. The entire process is carried out under nitrogen protection.

Microscopy

For scanning electron microscope (SEM) observation, cells were carefully harvested without stir. Following centrifugation (4000 g, 2 min), the supernatant was removed and the pellet was fixed

FIGURE 1 | Methane production from acetate in the 1st **(A)**, 4th **(B)**, 7th **(C)**, and 10th **(D)** transfer of wetland enrichment in the presence (nanoFe₃O₄) and absence (CK) of nanoFe₃O₄. The 1st transfer were inoculated from the pre-incubated soil slurry and the later transfers were inoculated always from the previous nanoFe₃O₄-amended transfer. The concentration of CH₄ produced was expressed as micromole per liter (mM) of the incubation medium. The error bars indicate the standard deviations of three replications.

FIGURE 2 | Methane production and acetate consumption in the ^{13}C isotope experiments with the 14th transfer enrichment. The sodium acetate-2-^{13}C (^{13}CH$_3$COONa) was used for the labeling treatment. The total concentrations of acetate and CH$_4$ were colored in green and black, respectively **(A,C)**. The ^{13}CH$_4$ percentages in total CH$_4$ and ^{13}CO$_2$ percentages in total CO$_2$ were colored in black and red, respectively **(B,D)**. The error bars indicate the standard deviations of three replicates.

with 2.5% (wt/vol) glutaraldehyde, dehydrated using a graded series of ethanol solutions, and dried with t-butanol. The samples were mounted on copper stubs, coated with platinum, and then imagined using JEOL S-4800 (JEOL, Japan). For transmission electron microscope (TEM) analysis, the fixed cells were sent to Beijing Zhongkebaice Technology Service Co., Ltd. to make ultrathin sections, and the morphology and structure of the samples were observed by G2F20 (200 KV) for the regions or particles of interest.
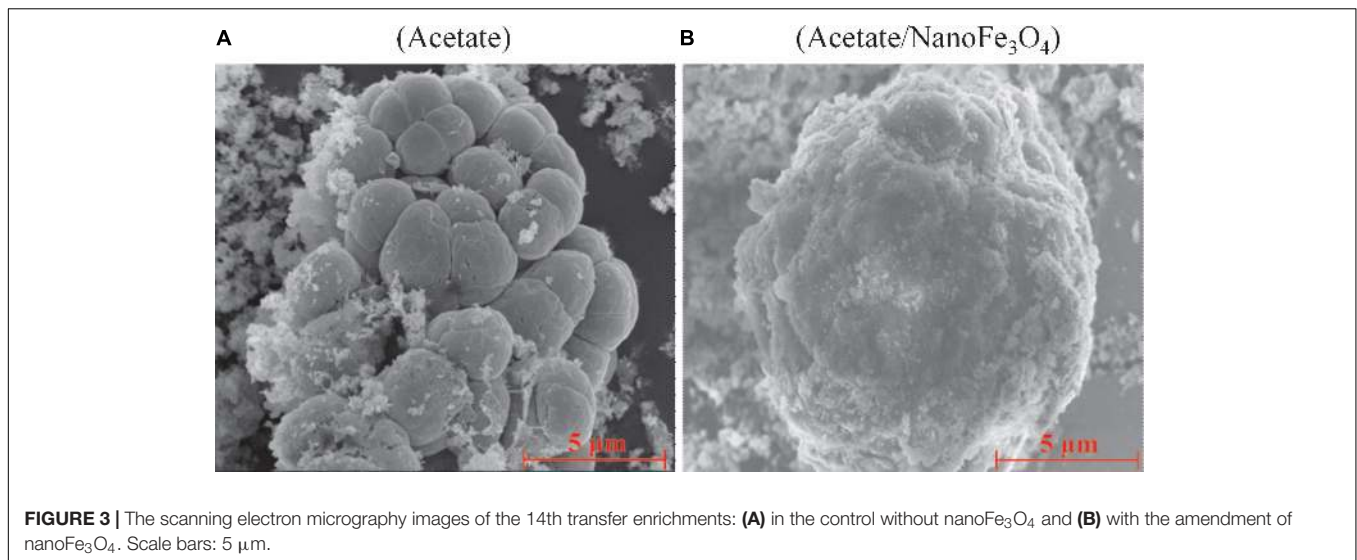
Chemical Analyses

Gas samples (0.1 mL) were regularly taken from headspace of incubations with a pressure-lock precision analytical syringe (Baton Rouge, LA, United States). The concentrations of CH$_4$ and CO$_2$ were analyzed using gas chromatographs GC-7890 (Agilent Technologies, United States) equipped with a thermal conductivity detector (Fu et al., 2018). Liquid samples (0.5 mL)

were taken with sterile syringes and centrifuged for 15 min at 17,949 × g at 4°C. The supernatant was collected, passed through 0.22-μm-pore-size filters, and analyzed for the concentrations of acetate and butyrate with an HPLC-1200 using a Zorbax SB-AQ C$_{18}$ column (Agilent Technologies, United States) (Fu et al., 2018). Redox potential (ORP) were measured with an Unisense redox microelectrode RD 100 (Unisense, Denmark).

RESULTS

NanoFe$_3$O$_4$ Specifically Promoted Acetotrophic Methanogenesis in Enrichment Cultures

The production of CH$_4$ occurred without lag in the first transfer indicating the ready activity of acetate oxidation in this wetland sediment (**Figure 1A**). Addition of 5 mM acetate yielded about

FIGURE 3 | The scanning electron micrography images of the 14th transfer enrichments: **(A)** in the control without nanoFe$_3$O$_4$ and **(B)** with the amendment of nanoFe$_3$O$_4$. Scale bars: 5 μm.

3.78 ± 0.13 mM CH$_4$ (normalized to liquid volume) in the first transfer (**Figure 1A**). When the concentration of acetate was increased to 10 mM, about 8.13 ± 0.12 mM of CH$_4$ was obtained in the later transfers (**Figures 1B–D**). These results indicated that CH$_4$ accumulated in the headspace corresponded to 80% of theoretical stoichiometric prediction of complete conversion of acetate to CH$_4$ and CO$_2$. Addition of nanoFe$_3$O$_4$ did not influence this conversion efficiency. However, nanoFe$_3$O$_4$ significantly accelerated the CH$_4$ production rate, with shorter lags and greater maximal rates compared with the control. For the 4th transfer, CH$_4$ production displayed a long lag in the control while it took less than a week before the onset of rapid production in the presence of nanoFe$_3$O$_4$ (**Figures 1B–D**).

Isotopic and chemical analysis was conducted during the labeling experiment at the 14th transfer. Incubations with or without labeling showed identical patterns of acetate consumption and CH$_4$ production (**Figure 2A** without and **Figure 2C** with isotopic labeling). In consistence with the early transfer incubation experiments, the addition of 10 mM acetate produced about 8.1–8.9 mM CH$_4$ (**Figures 2A,C**). When the sodium acetate-2-^{13}C (99 atom%; Sigma-Aldrich) was added as the substrate, the carbon isotopic ratios (δ^{13}C values) of CH$_4$ increased rapidly in the presence of nanoFe$_3$O$_4$, peaked at 40 ± 2.5% on the 9th day of culture (**Figure 2D**). However, the δ^{13}C values of CO$_2$ for the control (1.3 ± 0.04%) only slightly increased (**Figure 2B**). These results indicated that CH$_4$ was mainly produced from direct acetate cleavage. In the direct pathway, acetotrophic methanogens like *Methanosarcina* and *Methanosaeta* convert acetate into CH$_4$ and CO$_2$ (^{13}CH$_3$COOH $\rightarrow$ ^{13}CH$_4$ + CO$_2$). However, in the syntrophic pathway, acetate is oxidized to H$_2$ and CO$_2$ (^{13}CH$_3$COOH + 2H$_2$O $\rightarrow$ 4H$_2$ + ^{13}CO$_2$ + ^{12}CO$_2$). H$_2$ is consumed by hydrogenotrophic methanogens to generate CH$_4$ (4H$_2$ + $^{12/13}$CO$_2$ $\rightarrow$ $^{12/13}$CH$_4$ + 2H$_2$O). If the system is dominated by the syntrophic pathway, considering that the headspace of the serum bottle was filled with N$_2$:CO$_2$ (80:20), the carbon isotopic ratios (δ^{13}C values) of CO$_2$ will increase, and the carbon isotopic ratios (δ^{13}C values) of CH$_4$ should be even lower than the carbon isotopic ratios (δ^{13}C values) of CO$_2$.

Scanning electron micrograph showed the aggregated cells in the control (**Figure 3A**) at the 14th transfer. With the addition of nanoFe$_3$O$_4$, the shell-like coat formed on microbial aggregates with nanoFe$_3$O$_4$$_-$coated surfaces (**Figure 3B**).

Methanosarcina spp. Are Highly Enriched in Enrichment Cultures Supplemented With NanoFe$_3$O$_4$

DNA-SIP, T-RFLP and clone sequence analyses were used to determine microbial composition of the enrichment cultures. DNA-SIP was performed by applying ^{13}C-labeled acetate (^{13}CH$_3$COONa). Almost identical pattern was observed in the distribution of the density-resolved DNA fragments along the buoyant density gradient for the control (**Figures 4A,C**) and the nanoFe$_3$O$_4$ treatment (**Figures 4B,D**). The distribution of the archaeal (**Figures 4A,B**) and bacterial (**Figures 4C,D**) DNA shifted to the heavier fractions in the labeled samples compared with the non-labeled control (**Figure 4**). These results indicated that both the archaeal and bacterial populations assimilated ^{13}C-labeled acetate.

Three major T-RFs were detected in the archaeal T-RFLP fingerprints (**Figures 5A,B**) of the density-resolved DNA. The 184 bp T-RF was predominant in all T-RFLP profiles, and its relative abundance was reduced only in heavier layers. Analysis of the clone sequences indicated that these T-RFs belonged to *Methanosarcina* (**Figures 6A,B**). The T-RFs detected in the bacterial T-RFLP fingerprints include: 167 bp, representing *Anaerovorax*; 182 bp, representing *Syntrophomonas*; 284 bp, representing *Veillonellaceae*; 305 and 470 bp, both representing *Clostridium*; 363 bp, representing *Cytophaga*; 430 bp, representing *Azonexus*. The 430 bp was predominant in all experimental treatments (**Figures 5C,D**). For the control without nanoFe$_3$O$_4$, 430 bp showed a trend of increasing first and then decreasing with the DNA buoyant density (**Figure 5C**); the

FIGURE 4 | Quantitative profiles of archaeal **(A,B)** and bacterial **(C,D)** 16S rRNA genes across density-gradient fractions in incubations with ^{13}C-labeled (red) acetate and the non-labeled control (black), in the presence **(B,D)** or absence **(A,C)** of nanoFe$_3$O$_4$. The gradient fractions, characterized by their buoyant densities were generated using CsTFA density gradient centrifugation of DNA.

305 and 167 bp was secondary dominated in the non-labeling and labeling treatments, respectively. For the nanoFe$_3$O$_4$ treatments, the 430 bp T-RF was predominant across density gradients; other T-RFs either declined or did not change with the DNA buoyant density (**Figure 5D**).

Two bacterial and two archaeal clone libraries were constructed, with one each for the control and nanoFe$_3$O$_4$ treatment, respectively. All the archaeal clone sequences from both the nanoFe$_3$O$_4$ treatment and the control were affiliated to the *Methanosarcinales* order, with *Methanosarcina barkri* as the closest pure culture relative (**Figures 6A,B**). Clone sequences indicated that the bacterial communities in the enrichments consisted mainly of *Syntrophomonas, Veillonellaceae, Anaerovorax, Clostridium, Cytophaga, Azonexus, Desulfovibrionaceae,* and *Saccharofermentans acetigenes* (**Figures 6C,D**). The sequences affiliated to *Azonexus* accounted for approximately 59% of total sequences in the nanoFe$_3$O$_4$ library (**Figure 6D**). By comparison, *Clostridium* accounted for

49%, followed by *Veillonellaceae* (15%), *Anaerovorax* (10%) and *Azonexus* (10%) in the control library (**Figure 6C**).

NanoFe$_3$O$_4$ Promote Acetotrophic Methanogenesis by Pure Cultures of *Methanosarcina barkeri*

Pure culture systems of *M. barkeri* were constructed with acetate as the sole substrate. Various tests were carried out to investigate the effect of nanoFe$_3$O$_4$ on the methangenesis of pure culture strains. NanoFe$_3$O$_4$ significantly promoted the production of methane and the consumption of acetate by *M. barkeri* (**Figure 7A**). The maximum methane production rate (V_{max}) was 6.15 ± 0.34 mmol/L·d in the presence of nanoFe$_3$O$_4$, which was about two times that of the control (2.91 ± 0.21 mmol/L·d). This rapid methanogenesis process occurred 10 days earlier than the control. However, the addition of nano-graphite (particle diameter: 35 nm) did not show any promoting effect. On the other hand, the addition of CNTs (outside diameter: 10–20 nm, length: 10–30 μm) retained a stimulatory effect that was less significant compared with nanoFe$_3$O$_4$ (**Figure 7F**).

Redox Activity Rather Than Electrical Conductivity of NanoFe$_3$O$_4$ Leads to Enhanced Methanogenesis by *M. barkeri*

In order to clarify the action sites of nanoFe$_3$O$_4$ on *M. barkeri*, we performed ultrathin sections of *M. barkeri* and TEM analysis. The results showed that the nanoFe$_3$O$_4$ existed in extracellular and intercellular spaces, cell surfaces, cell membranes, and the cytoplasms (**Figure 7B**). XRD was used to determine the possible structural changes of nanoFe$_3$O$_4$ during the culture process. The XRD pattern data showed no change in the crystal structure of nanoFe$_3$O$_4$ after culture (**Figure 7C**). The structure and composition of nanoFe$_3$O$_4$ were further analyzed with Raman spectroscopy on a microscopic scale. The Raman spectrum detected the production of hematite (compared to a Raman spectrum of hematite reported in the RRUFF data base[1]) after the incubation with *M. barkeri* (**Figure 7D**).

After the addition of nanoFe$_3$O$_4$, the oxidation-reduction potential (ORP) of the culture system was increased from −350 to −300 mV, but did not continue to increase as the concentration of nanoFe$_3$O$_4$ increased (**Figure 7E**). We performed a cyclic voltammogram (CV) scan of all pure culture methanogenic systems to analyze the redox activity changes of the systems. CV can reflect the redox activity and capacitance in the electrochemical reactor. The larger the capacitance, the more charge is stored in the system. As shown in **Figures 8A–D**, the capacitance of the bioreactors with nanoFe$_3$O$_4$ was higher than that of the control reactors, suggesting an enhanced redox activity. The capacitance of the bioreactors with nanoFe$_3$O$_4$ increased to the maximum on day 10 (**Figure 8B**) and then gradually decreased to the minimum on day 30 (**Figure 8D**), which was consistent with the methanogenic activity. By contrast, the capacitance of the control bioreactors without nanoFe$_3$O$_4$
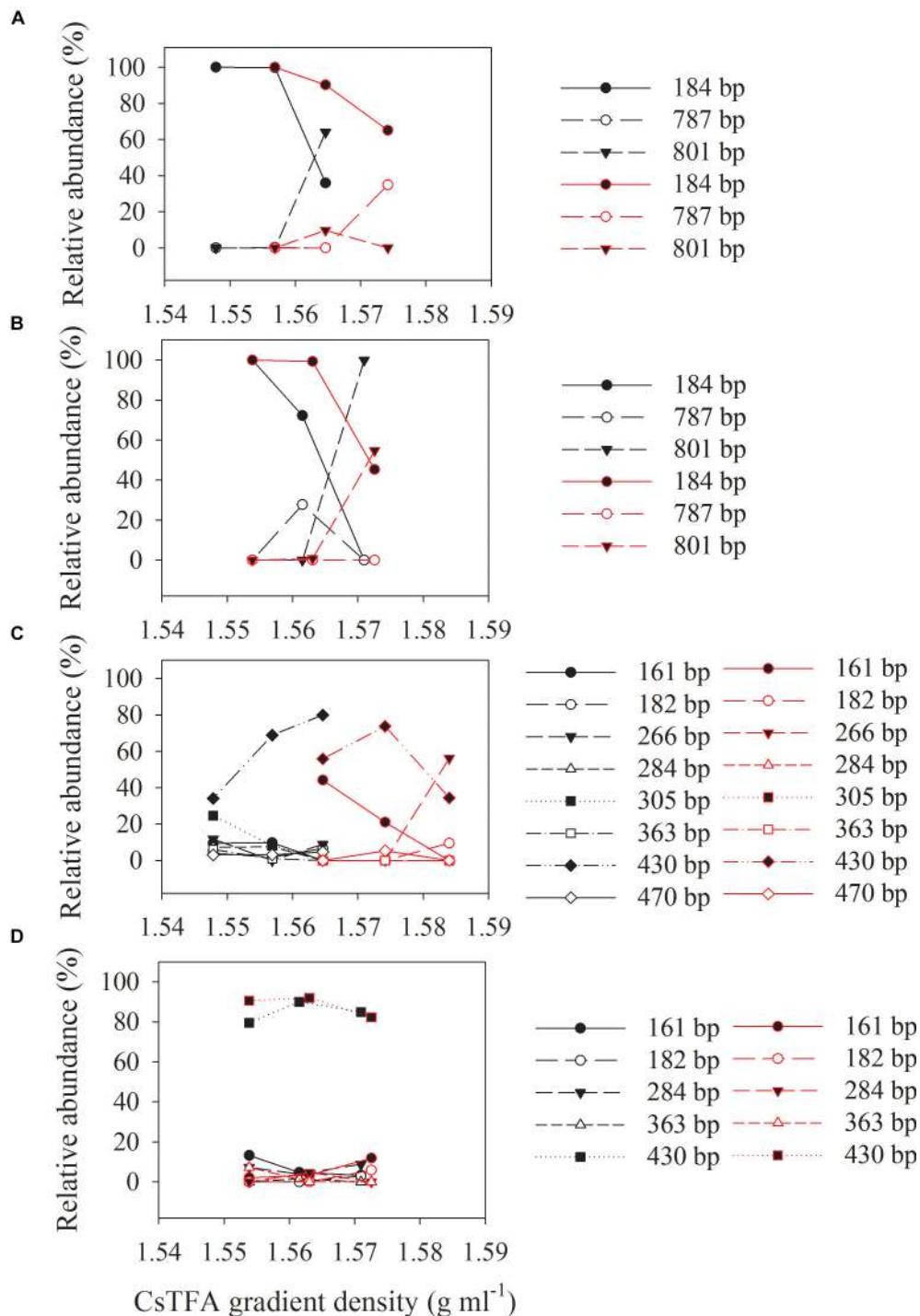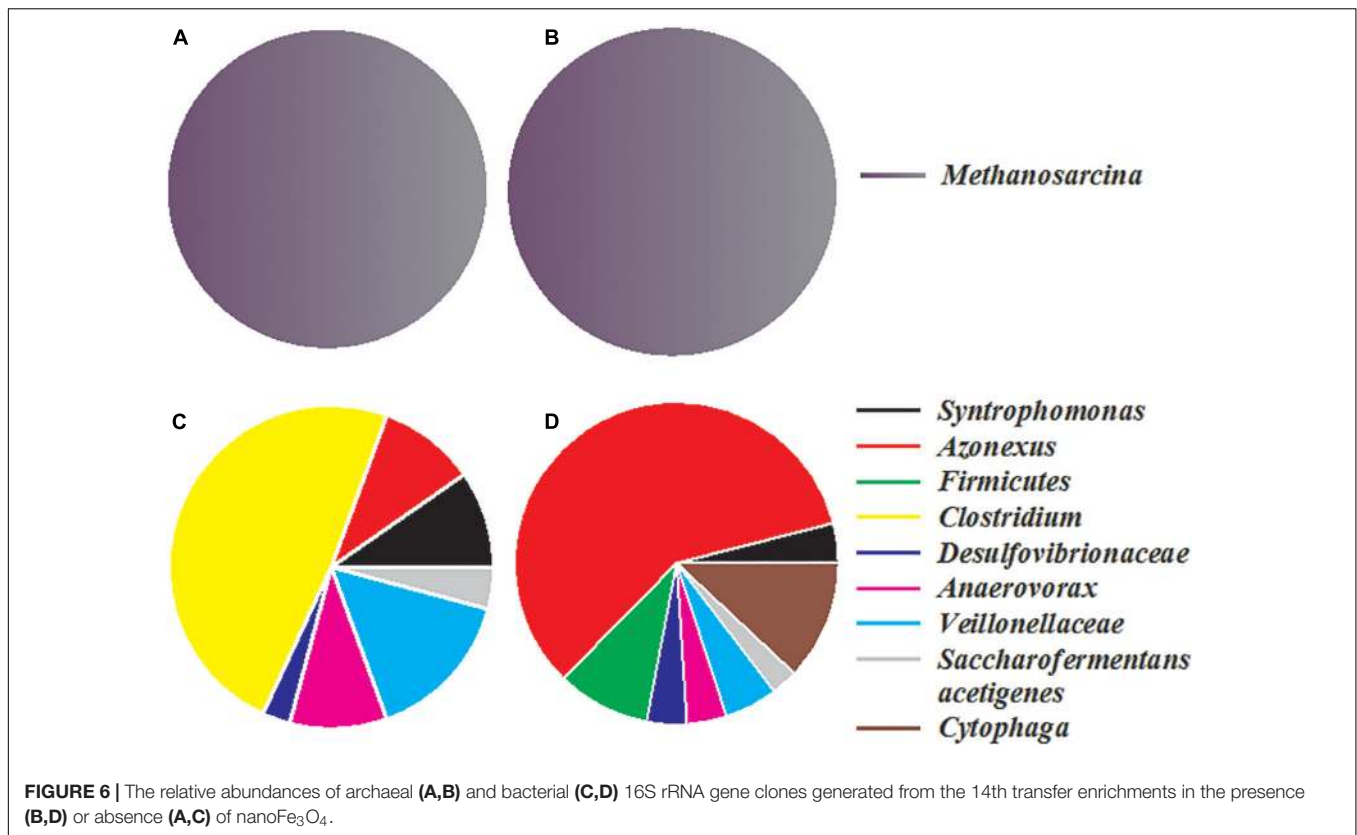
---

[1]http://rruff.info/hematite/display=default/R040024

FIGURE 5 | The relative abundances of archaeal **(A,B)** and bacterial **(C,D)** T-RFs in the density-resolved DNA fractions in incubations with ^{13}C-labeled (red) acetate and the non-labeled control (black), in the presence **(B,D)** or absence **(A,C)** of nanoFe$_3$O$_4$. The gradient fractions, characterized by their buoyant densities were generated using CsTFA density gradient centrifugation of DNA.

kept relatively stable during the 30-days cultivation. Moreover, a pair of oxidation and reduction peaks with a mid-point potential of approximately −200 mV vs. SHE appeared in the CV scans for both treatments. However, the peaks disappeared

for the bioreactors with nanoFe$_3$O$_4$ on day 30. This indicated the redox transformation of certain redox-active species in the bioreactors with nanoFe$_3$O$_4$. EIS was used to evaluate the electron transfer resistance of the reactors, which was crucial

FIGURE 6 | The relative abundances of archaeal **(A,B)** and bacterial **(C,D)** 16S rRNA gene clones generated from the 14th transfer enrichments in the presence **(B,D)** or absence **(A,C)** of nanoFe$_3$O$_4$.

for the charge transfer efficiency. As shown in **Figures 8E–H**, the addition of nanoFe$_3$O$_4$ significantly decreased the electron transfer resistance (R$_{ct}$ = 37.7 Ω) compared with the control reactors (R$_{ct}$ = 353.5 Ω) at day 0. Although the electron transfer resistances of the control reactors decreased to 68.9 Ω after 30-days cultivation it was still higher than that for the nanoFe$_3$O$_4$ treatment (27.6 Ω). The decreasing R$_{ct}$ over time might be due to the adsorption of *M. barkeri* on the electrode surfaces.

DISCUSSION

Redox Behavior of Magnetite in NanoFe$_3$O$_4$/*M. barkeri* Interface

Previous literatures have reported that conductive materials such as nanoFe$_3$O$_4$, graphite, CNTs, activated carbon, etc., can promote the methane production via mediating DIET. However, few studies have focused on the effects of these materials on methanogens themselves. This work evaluated the effects of nanoFe$_3$O$_4$ in enrichment cultures initiated with wetland soils with acetate as a substrate. Compared with the control, the addition of nanoFe$_3$O$_4$ consistently shortened the lag period and enhanced the maximum rate of CH$_4$ production. Highly enriched methanogens were obtained through continuous transfers in the presence of nanoFe$_3$O$_4$. Mass balance and isotopic labeling indicated that the conversion of acetate conformed to the formula: CH$_3$COOH → CH$_4$ + CO$_2$. Molecular analyses revealed that *Methanosarcina* closely related to a *M. bakeri* strain

were left as the only methanogen in the enrichment. These results suggested that nanoFe$_3$O$_4$ played an important role in the acetotrophic methanogenesis (**Figure 9**). Such a promoting effect of nanoFe$_3$O$_4$ was further confirmed in pure culture of *M. bakeri*.

Different mechanisms may be involved in the promoting effect of nanoFe$_3$O$_4$/*M. bakeri* system. Firstly, nanoFe$_3$O$_4$ has a relatively low redox potential (−314 mV) (Straub et al., 2001). It has been argued that the stimulatory effect by nanomaterials like CNTs on syntrophic coculture and pure culture of methanogens is caused by the decrease in redox potential (Salvador et al., 2017). Similar effect may be postulated for nanoFe$_3$O$_4$. However, the experimental results showed that the ORP of the system increased about 50 mV after the addition of nanoFe$_3$O$_4$ (**Figure 7E**). Therefore, this inference was untenable here.

Our previous research suggested that the electrical conductivity of nanomaterials played the key role in promoting the syntrophic oxidation of butyrate (Li et al., 2015; Fu et al., 2018). However, the results of this study showed that graphite and CNTs with higher conductivity did not have the similar promoting effect like nanoFe$_3$O$_4$ (**Figure 7F**). Apart from the common property in electric conductivity, nanoFe$_3$O$_4$, CNTs and graphite are chemically and physically different. It was probable that a certain special property of nanoFe$_3$O$_4$ rather than the conductivity played a decisive role.

The system's CV scan results showed that the redox activity was highly consistent with the methanogenic activity. The
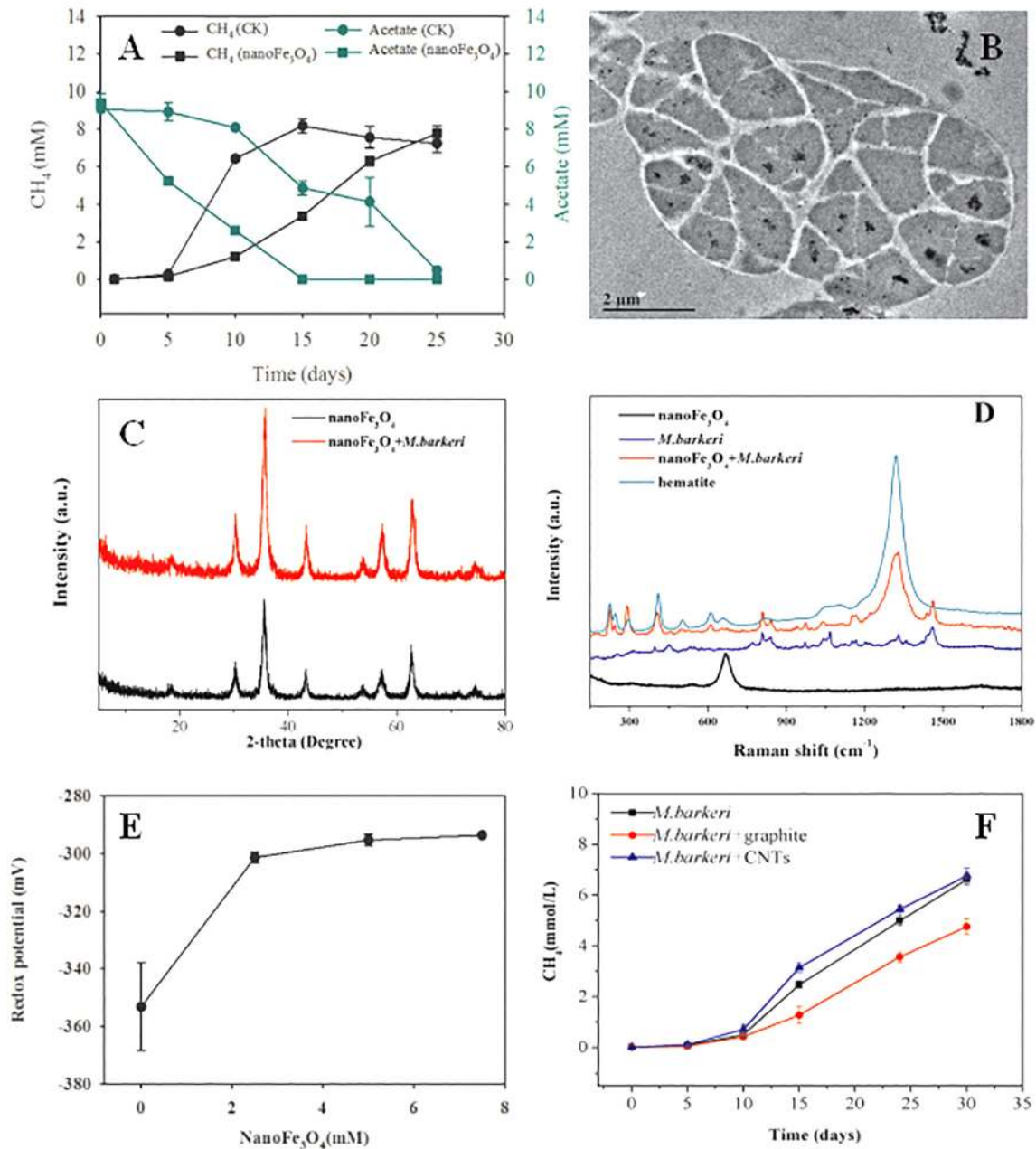
FIGURE 7 | Effect of nanoFe$_3$O$_4$ on CH$_4$ production by *M. barkeri*. **(A)** The total concentrations of CH$_4$ (black) and acetate (green) with nanoFe$_3$O$_4$ (circle) or without nanoFe$_3$O$_4$ (square). **(B)** the transmission electron microscope (TEM) image of ultrathin sections of *M. barkeri* with the amendment of nanoFe$_3$O$_4$. **(C)** The X ray diffraction spectrum of nanoFe$_3$O$_4$ before the incubation without *M. barkeri* (black) and after the incubation with *M. barkeri* (red). **(D)** The Raman spectrum of *M. barkeri* (blue), nanoFe$_3$O$_4$ before the incubation without *M. barkeri* (black) and after the incubation with *M. barkeri* (red). **(E)** Oxidation-reduction potential (ORP) changes in medium with different concentrations of nanoFe$_3$O$_4$. **(F)** Methane production from acetate by *M. barkeri*. Three treatments were applied with the additions of: graphite nanoparticles (*M. barkeri* + Graphite), carbon nanotubes (*M. barkeri* + CNTs), and the control without nanomaterials (*M. barkeri*). The error bars indicate the standard deviations of three replicates.

addition of nanoFe$_3$O$_4$ significantly increased the redox activity of the system (**Figures 8A–D**). Since soluble electron shuttle molecule was not present in our system, the CV measurement could reflect the activities of the enzymes that catalyzed the electron transport in the membrane. In other words, the higher

catalytic currents could be an indicator of a better redox enzyme activity. As shown in **Figures 8A–D**, the catalytic currents for the nanoFe$_3$O$_4$ treatment increased in the first 10 days and then gradually decreased to the background at day 30. This means that the redox enzyme activities in the
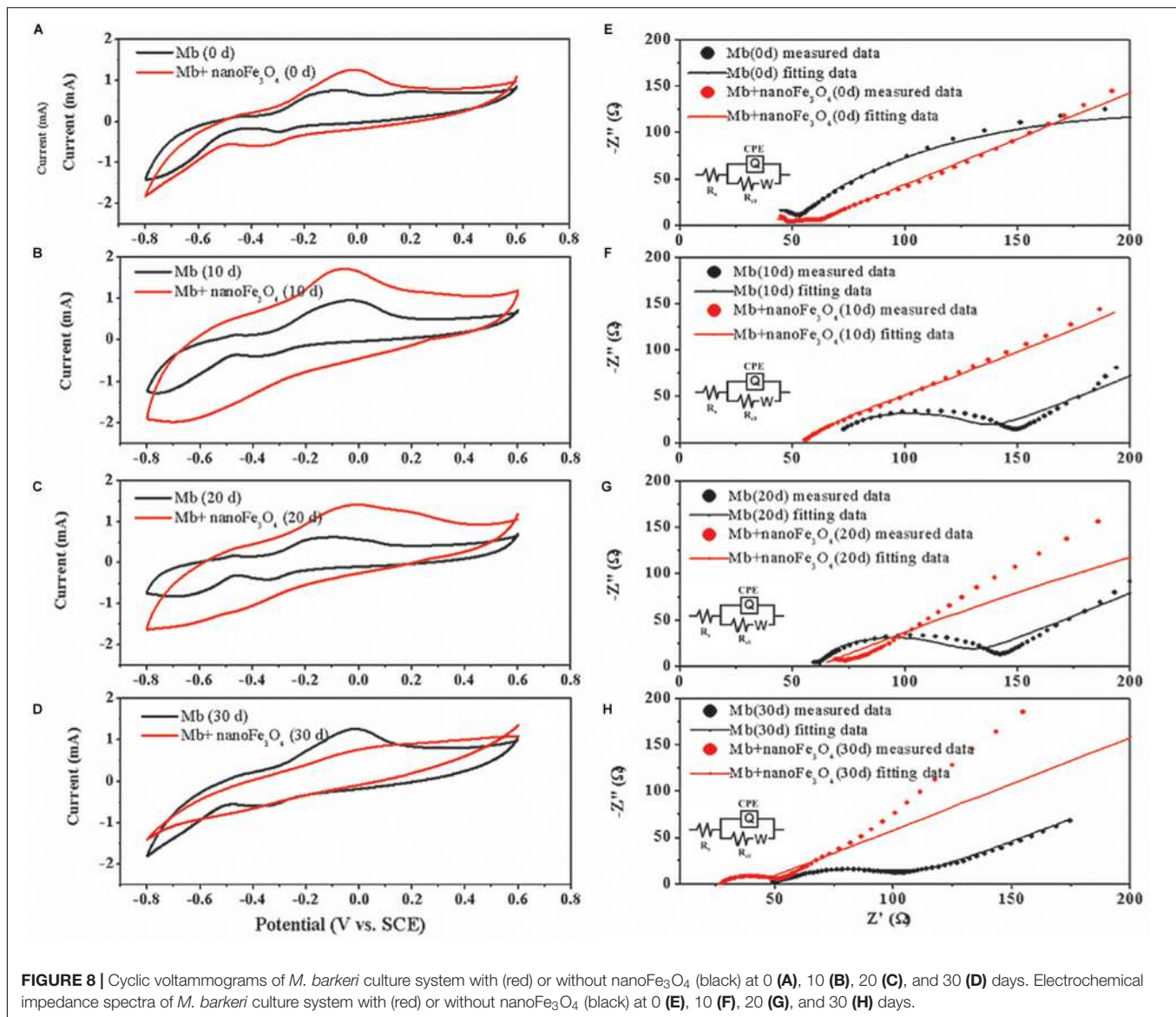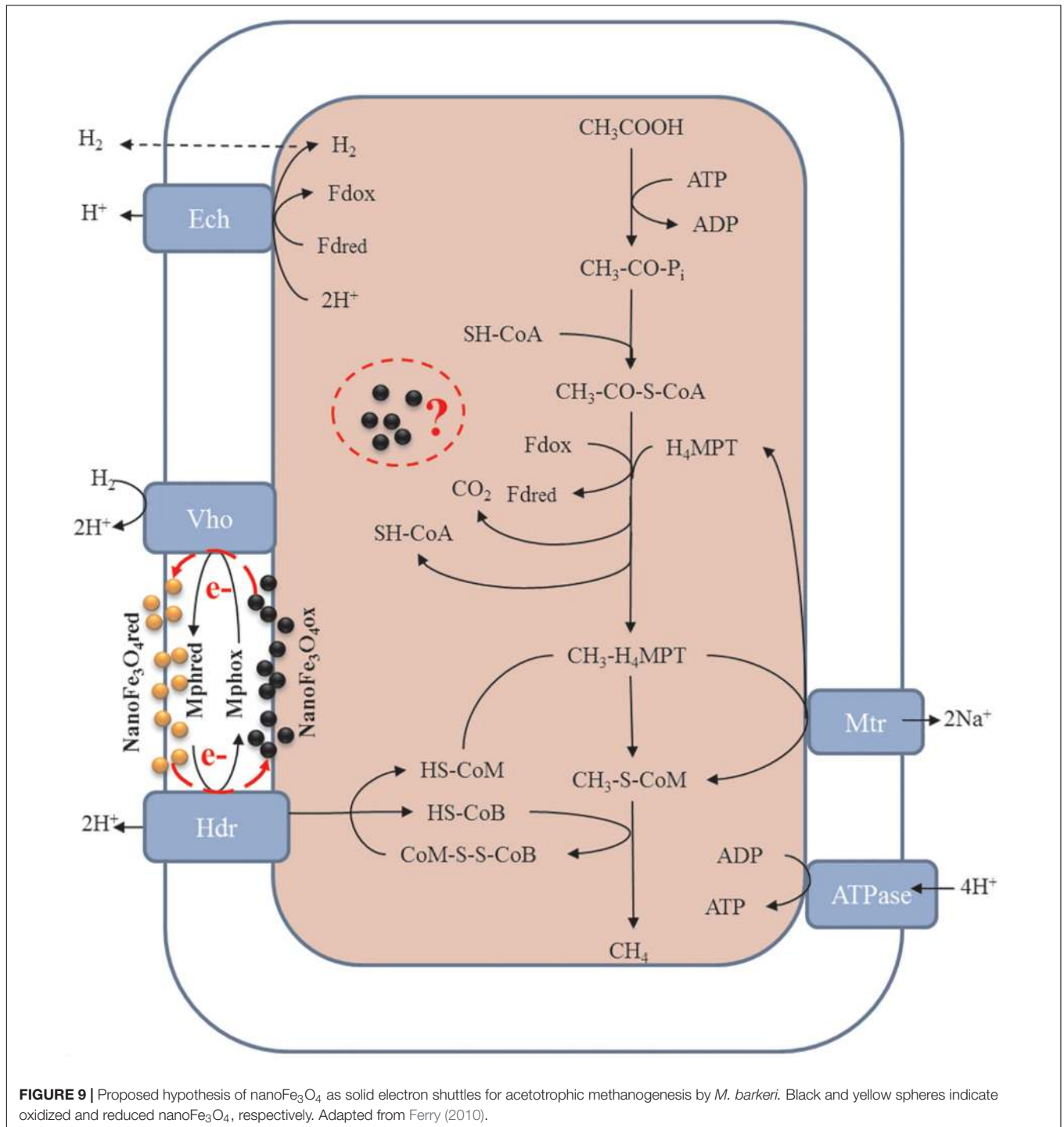
FIGURE 8 | Cyclic voltammograms of *M. barkeri* culture system with (red) or without nanoFe$_3$O$_4$ (black) at 0 **(A)**, 10 **(B)**, 20 **(C)**, and 30 **(D)** days. Electrochemical impedance spectra of *M. barkeri* culture system with (red) or without nanoFe$_3$O$_4$ (black) at 0 **(E)**, 10 **(F)**, 20 **(G)**, and 30 **(H)** days.

membrane were the highest in the middle period of the experiments. The detection of hematite by Raman further indicated that nanoFe$_3$O$_4$ did undergo a redox transformation on the microcosmic scale (**Figure 7D**). Based on this, we can infer that nanoFe$_3$O$_4$ participate in the electron transfer on the membrane of *M. bakeri*.

NanoFe$_3$O$_4$ as Solid-State Electron Shuttles for Enhanced Acetotrophic Methanogenesis

Acetate is the worst substrate for methanogenesis with a standard free energy change of only -36 kJ mol^{-1}. It can be only used by cytochrome-containing methanogens such as *Methanosarcina acetivorans, Methanosarcina mazei, and Methanosarcina barkeri* (Thauer et al., 2008; Welte and Deppenmeier, 2014). To conserve the little energy available as much as possible, acetotrophic

methanogens have evolved a sophisticated metabolic pathway (**Figure 9**). In the pathway, CH$_3$COOH reacts with sulfhydryl-containing coenzyme A (SH-CoA) to form CH$_3$-CO-S-CoA. This is an endergonic reaction. Then, the carboxyl group combines with the oxidized ferredoxin (Fd$_{ox}$) to form a reduced ferredoxin (Fd$_{red}$), and releases CO$_2$ and regenerates SH-CoA. The methyl moiety combines with tetrahydromethanopterin (H$_4$MPT) to form CH$_3$-H4MPT, which reacts with sulfhydryl-containing coenzyme M (HS-CoM) to form CH$_3$-S-MPT and H$_4$MPT. Then CH$_3$-S-MPT reacts with sulfhydryl-containing coenzyme B (HS-CoB) to form CH$_4$ and heterodisulfide of CoM and CoB (CoM-S-S-CoB) (Costa and Leigh, 2014; Welte and Deppenmeier, 2014). In *Methanosarcina* species, Fd$_{red}$ is used to produce H$_2$ by ferredoxin-dependent hydrogenase (Ech). The H$_2$ diffuses across the cell membrane and is oxidized by methanophenazine-dependent hydrogenase (Vht) to reduce a membrane-bound methanophenazine (Mph). The

FIGURE 9 | Proposed hypothesis of nanoFe$_3$O$_4$ as solid electron shuttles for acetotrophic methanogenesis by *M. barkeri*. Black and yellow spheres indicate oxidized and reduced nanoFe$_3$O$_4$, respectively. Adapted from Ferry (2010).

reduced Mph delivers electrons to the membrane-bound heterodisulfide reductase (HdrDE) to regenerate free CoM and CoB from the CoM-S-S-CoB (Kulkarni et al., 2018; Lovley, 2018; Mand et al., 2018).

Mph is a unique membrane electron carrier found in *Methanosarcina* species (Beifuss et al., 2000). The Mph-catalyzed step is rate limiting in the central metabolism of acetate. Mph has a lower redox potential (-150 mV). The content of Mph

in *M. acetivorans* were threefold higher than that in *M. barkeri* (Duszenko and Buan, 2017). This suggests the cell membrane of *M. acetivorans* is electrically quantized as if it were a single conductive metal sheet and near optimal for electron transport (Duszenko and Buan, 2017). Therefore, in theory, by adding an electron carrier with a function similar to Mph to the medium, the acetotrophic methanogenic rate of *M. barkeri* can be increased. Beckmann et al. have demonstrated that soluble

neutral red (−375 mV) delivers reducing equivalents directly to the membrane bound HdrED of *Methanosarcina* species, and thus increases the rates of proton translocation and regeneration of the methanogenic cofactors CoM-SH and CoB-SH (Beckmann et al., 2016). This was the first report that an artificial electron shuttle can mimic the membrane integrated electron shuttle Mph.

Although nanoFe₃O₄ (−314 mV) existed in solid state, the results of ultrathin sections proved that nanoFe₃O₄ passed through the cell membrane of *M. barkeri*, so nanoFe₃O₄ could function as electron shuttles like soluble neutral red. It was worth mentioning that nanoFe₃O₄ did not show any effect on CH₄ production by two hydrogenotrophic methanogens *Methanococcus maripaludis* and *Methanocella conradii* (Fu et al., 2018). The most essential difference between them and *M. barkeri* was the lack of electron transport chain on the membrane (Thauer et al., 2008; Costa and Leigh, 2014; Welte and Deppenmeier, 2014). Based on the characteristics and performance of nanoFe₃O₄, we propose the hypothesis that nanoFe₃O₄ may act as solid-state electron shuttles that performs a similar function like Mph. Here we also emphasize that this may not be the only mechanism by which nanoFe₃O₄ stimulates methane production. Other unknown biochemical activities may influence methanogenesis. Our experimental evidence has clarified that a large amount of nanoFe₃O₄ passes through the cell membrane and enters the cytoplasm. What changes may occur in this part of the nanoFe₃O₄, what reactions they may participate in, and what kind of effects on the organism, we don't know anything about these issues and deserve further study.

DATA AVAILABILITY

The datasets generated for this study can be found in GenBank, MK061905–MK062157.

AUTHOR CONTRIBUTIONS

SZ and YL conceived the research. LF performed the enrichment cultivation, isotope labeling, and molecular analysis. TZ and JW performed the pure culture test. LpY performed the electrochemical analysis. LxY performed the Raman analysis. LF wrote the manuscript. LF and LpY edited the manuscript. All authors reviewed and approved the manuscript.

FUNDING

REFERENCES

Beckmann, S., Welte, C., Li, X., Oo, Y. M., Kroeninger, L., Heo, Y., et al. (2016). Novel phenazine crystals enable direct electron transfer to methanogens in anaerobic digestion by redox potential modulation. *Energy Environ. Sci.* 9, 644–655. doi: 10.1039/C5EE03085D

Beifuss, U., Tietze, M., Bäumer, S., and Deppenmeier, U. (2000). Methanophenazine: structure, total synthesis, and function of a new cofactor from methanogenic *archaea*. *Angew. Chem. Int. Ed.* 39, 2470–2472. doi: 10.1002/1521-3773(20000717)39:14<2470::AID-ANIE2470>3.0.CO;2-R

Costa, K. C., and Leigh, J. A. (2014). Metabolic versatility in methanogens. *Curr. Opin. Biotechnol.* 29, 70–75. doi: 10.1016/j.copbio.2014.02.012

Duszenko, N., and Buan, N. R. (2017). Physiological evidence for isopotential tunneling in the electron transport chain of methane-producing *Archaea*. *Appl. Environ. Microbiol.* 83, AEM.00950–AEM.01017. doi: 10.1128/AEM.00950-17

Ferry, J. G. (2010). CO in methanogenesis. *Ann. Microbiol.* 60, 1–12. doi: 10.1007/s13213-009-0008-5

Fleet, M. (1981). The structure of magnetite. *Acta Crystallograp. Sec. B* 37, 917–920. doi: 10.1107/S0567740881004597

Fu, L., Song, T., and Lu, Y. (2015). Snapshot of methanogen sensitivity to temperature in zoige wetland from tibetan plateau. *Front. Microbiol.* 6:131. doi: 10.3389/fmicb.2015.00131

Fu, L., Song, T., Zhang, W., Zhang, J., and Lu, Y. (2018). Stimulatory effect of magnetite nanoparticles on a highly enriched butyrate-oxidizing consortium. *Front. Microbiol.* 9:1480. doi: 10.3389/fmicb.2018.01480

Gan, Y., Qiu, Q., Liu, P., Rui, J., and Lu, Y. (2012). Syntrophic oxidation of propionate in rice field soil at 15 and 30 C under methanogenic conditions. *Appl. Environ. Microbiol.* 78, 4923–4932. doi: 10.1128/AEM.00688-12

Hao, L. P., Lü, F., He, P. J., Li, L., and Shao, L. M. (2010). Predominant contribution of syntrophic acetate oxidation to thermophilic methane formation at high acetate concentrations. *Environ. Sci. Technol.* 45, 508–513. doi: 10.1021/es102228v

Hudson, R., Feng, Y., Varma, R. S., and Moores, A. (2014). Bare magnetic nanoparticles: sustainable synthesis and applications in catalytic organic transformations. *Green Chem.* 16, 4493–4505. doi: 10.1039/C4GC00418C

Jing, Y., Wan, J., Angelidaki, I., Zhang, S., and Luo, G. (2017). iTRAQ quantitative proteomic analysis reveals the pathways for methanation of propionate facilitated by magnetite. *Water Res.* 108, 212–221. doi: 10.1016/j.watres.2016.10.077

Kang, Y. S., Risbud, S., Rabolt, J. F., and Stroeve, P. (1996). Synthesis and characterization of nanometer-size Fe3O4 and γ-Fe2O3 particles. *Chem. Mater.* 8, 2209–2211. doi: 10.1021/cm960157j

Kato, S., Hashimoto, K., and Watanabe, K. (2012). Methanogenesis facilitated by electric syntrophy via (semi)conductive iron-oxide minerals. *Environ. Microbiol.* 14, 1646–1654. doi: 10.1111/j.1462-2920.2011.02611.x

Kulkarni, G., Mand, T. D., and Metcalf, W. W. (2018). Energy conservation via hydrogen cycling in the methanogenic *Archaeon Methanosarcina barkeri*. *Mbio* 9, e01256–e1318. doi: 10.1128/mBio.01256-18

Kumar, S., Stecher, G., and Tamura, K. (2016). MEGA7: Molecular evolutionary genetics analysis version 7.0 for bigger datasets. *Mol. Biol. Evol.* 33, 1870–1874. doi: 10.1093/molbev/msw054

Li, H., Chang, J., Liu, P., Fu, L., Ding, D., and Lu, Y. (2015). Direct interspecies electron transfer accelerates syntrophic oxidation of butyrate in paddy soil enrichments. *Environ. Microbiol.* 17, 1533–1547. doi: 10.1111/1462-2920.12576

Liu, P., Qiu, Q., and Lu, Y. (2011). Syntrophomonadaceae-affiliated species as active butyrate-utilizing syntrophs in paddy field soil. *Appl. Environ. Microbiol.* 77, 3884–3887. doi: 10.1128/AEM.00190-11

Lovley, D. R. (2017). Syntrophy goes electric: direct interspecies electron transfer. *Ann. Rev. Microbiol.* 71, 643–664. doi: 10.1146/annurev-micro-030117-020420

Lovley, D. R. (2018). The hydrogen economy of *Methanosarcina barkeri*: life in the fast lane. *J. Bacteriol.* 200, e00445–e00518. doi: 10.1128/JB.00445-18

Lü, Z., and Lu, Y. (2012). *Methanocella conradii* sp nov., a thermophilic, obligate hydrogenotrophic methanogen, isolated from chinese rice field soil. *PLoS One* 7:e35279. doi: 10.1371/journal.pone.0035279

Ma, K., Conrad, R., and Lu, Y. (2012). Responses of methanogen mcrA genes and their transcripts to an alternate dry/wet cycle of paddy field soil. *Appl. Environ. Microbiol.* 78, 445–454. doi: 10.1128/AEM.06934-11

Mand, T. D., Kulkarni, G., and Metcalf, W. W. (2018). Genetic, biochemical, and molecular characterization of *Methanosarcina barkeri* mutants lacking three distinct classes of hydrogenase. *J. Bacteriol.* 200:16. doi: 10.1128/JB.00342-18

Mohammed, L., Gomaa, H. G., Ragab, D., and Zhu, J. (2017). Magnetic nanoparticles for environmental and biomedical applications: a review. *Particuology* 30, 1–14. doi: 10.1016/j.partic.2016.06.001

Rotaru, A.-E., Shrestha, P. M., Liu, F., Markovaite, B., Chen, S., Nevin, K. P., et al. (2014). Direct interspecies electron transfer between *Geobacter metallireducens* and *Methanosarcina barkeri*. *Appl. Environ. Microbiol.* 80, 4599–4605. doi: 10.1128/AEM.00895-14

Rui, J., Qiu, Q., and Lu, Y. (2011). Syntrophic acetate oxidation under thermophilic methanogenic condition in chinese paddy field soil. *Fems Microbiol. Ecol.* 77, 264–273. doi: 10.1111/j.1574-6941.2011.01104.x

Salvador, A. F., Martins, G., Melle-Franco, M., Serpa, R., Stams, A. J. M., Cavaleiro, A. J., et al. (2017). Carbon nanotubes accelerate methane production in pure cultures of methanogens and in a syntrophic coculture. *Environ. Microbiol.* 19, 2727–2739. doi: 10.1111/1462-2920.13774

Schnürer, A., Zellner, G., and Svensson, B. H. (1999). Mesophilic syntrophic acetate oxidation during methane formation in biogas reactors. *FEMS Microbiol. Ecol.* 29, 249–261. doi: 10.1016/S0168-6496(99)00016-1

Straub, K. L., Benz, M., and Schink, B. (2001). Iron metabolism in anoxic environments at near neutral pH. *FEMS Microbiol. Ecol.* 34, 181–186. doi: 10.1111/j.1574-6941.2001.tb00768.x

Su, C. (2017). Environmental implications and applications of engineered nanoscale magnetite and its hybrid nanocomposites: a review of recent literature. *J. Hazard. Mater.* 322, 48–84. doi: 10.1016/j.jhazmat.2016.06.060

Tang, J., Zhuang, L., Ma, J., Tang, Z., Yu, Z., and Zhou, S. (2016). Secondary mineralization of ferrihydrite affect microbial methanogenesis in geobacter/methanosarcina co-cultures. *Appl. Environ. Microbiol.* 82, AEM.01517–1616. doi: 10.1128/AEM.01517-16

Thauer, R. K., Kaster, A.-K., Seedorf, H., Buckel, W., and Hedderich, R. (2008). Methanogenic archaea: ecologically relevant differences in energy conservation. *Nat. Rev. Microbiol.* 6, 579–591. doi: 10.1038/nrmicro1931

Viggi, C. C., Rossetti, S., Fazi, S., Paiano, P., Majone, M., and Aulenta, F. (2014). Magnetite particles triggering a faster and more robust syntrophic pathway of methanogenic propionate degradation. *Environ. Sci. Technol.* 48, 7536–7543. doi: 10.1021/es5016789

Welte, C., and Deppenmeier, U. (2014). Bioenergetics and anaerobic respiratory chains of aceticlastic methanogens. *Biochim. Et Biophys. Acta Bioenerg.* 1837, 1130–1147. doi: 10.1016/j.bbabio.2013.12.002

Yamada, C., Kato, S., Ueno, Y., Ishii, M., and Igarashi, Y. (2015). Conductive iron oxides accelerate thermophilic methanogenesis from acetate and propionate. *J. Biosci. Bioeng.* 119, 678–682. doi: 10.1016/j.jbiosc.2014.11.001

Yang, Z., Xu, X., Guo, R., Fan, X., and Zhao, X. (2015). Accelerated methanogenesis from effluents of hydrogen-producing stage in anaerobic digestion by mixed cultures enriched with acetate and nano-sized magnetite particles. *Biores. Technol.* 190, 132–139. doi: 10.1016/j.biortech.2015.04.057

Zhang, J., and Lu, Y. (2016). Conductive Fe3O4 nanoparticles accelerate syntrophic methane production from butyrate oxidation in two different lake sediments. *Front. Microbiol.* 7:1316. doi: 10.3389/fmicb.2016.01316

Zhou, S., Tang, J., Yuan, Y., Yang, G., and Xing, B. (2018). TiO2 nanoparticle-induced nanowire formation facilitates extracellular electron transfer. *Environ. Sci. Technol. Lett.* 5, 564–570. doi: 10.1021/acs.estlett.8b00275

Zhuang, L., Ma, J., Yu, Z., Wang, Y., and Tang, J. (2018). Magnetite accelerates syntrophic acetate oxidation in methanogenic systems with high ammonia concentrations. *Microb. Biotechnol.* 11, 710–720. doi: 10.1111/1751-7915.13286

Zhuang, L., Tang, J., Wang, Y., Hu, M., and Zhou, S. (2015). Conductive iron oxide minerals accelerate syntrophic cooperation in methanogenic benzoate degradation. *J. Hazard. Mater.* 293, 37–45. doi: 10.1016/j.jhazmat.2015.03.039